MATERIALS SCIENCE

Ideal plasticity and shape memory of nanolamellar high-entropy alloys

Shuai Chen[1,2]†, Ping Liu[2]†, Qingxiang Pei[2], Zhi Gen Yu[2], Zachary H. Aitken[2], Wanghui Li[2], Zhaoxuan Wu[3], Rajarshi Banerjee[4], David J. Srolovitz[5]*, Peter K. Liaw[6]*, Yong-Wei Zhang[2]*

Understanding the relationship among elemental compositions, nanolamellar microstructures, and mechanical properties enables the rational design of high-entropy alloys (HEAs). Here, we construct nanolamellar Al_x-CoCuFeNi HEAs with alternating high– and low–Al concentration layers and explore their mechanical properties using a combination of molecular dynamic simulation and density functional theory calculation. Our results show that the HEAs with nanolamellar structures exhibit ideal plastic behavior during uniaxial tensile loading, a feature not observed in homogeneous HEAs. This remarkable ideal plasticity is attributed to the unique deformation mechanisms of phase transformation coupled with dislocation nucleation and propagation in the high–Al concentration layers and the confinement and slip-blocking effect of the low–Al concentration layers. Unexpectedly, this ideal plasticity is fully reversible upon unloading, leading to a remarkable shape memory effect. Our work highlights the importance of nanolamellar structures in controlling the mechanical and functional properties of HEAs and presents a fascinating route for the design of HEAs for both functional and structural applications.

INTRODUCTION

Conventionally, metallic alloys are designed on the basis of one or two principal elements alloying with a number of minor elements, e.g., aluminum alloys (*1*), cobalt superalloys (*2*), nickel alloys (*3*), etc. In 2004, a previously unidentified type of alloys consisting of five or more principal elements, termed as high-entropy alloys (HEAs), has been innovatively proposed by Yeh *et al.* (*4*) and Cantor *et al.* (*5*). Since then, HEAs have attracted widespread attention because of their superior mechanical and functional properties (*6*–*8*), including a strength-ductility synergy beyond current benchmark ranges (*7*), excellent phase stability at elevated temperatures (*8*), etc. It is widely recognized that the mechanical properties of HEAs rely heavily on their compositions and micro/nanostructures (*9*, *10*). In multicomponent HEAs, there is an enormous number of different local atomic configurations, i.e., micro/nanostructures (*11*). Hence, an in-depth understanding of the composition-structure-property relationship of HEAs enables their rational design.

Several strategies have been proposed to maximize the mechanical properties of HEAs by tailoring their microstructures, e.g., introducing short-range ordering (SRO) in CoCrFeNiPd (*12*)/CoCuFeNiPd (*13*), $L1_2$ intermetallic nanoprecipitates into face-centered cubic (fcc) $(FeCoNi)_{86}$-Al_7Ti_7 (*14*)/$Fe_{25}Co_{25}Ni_{25}Al_{10}Ti_{15}$ (*15*), or body-centered tetragonal nanoprecipitates into body-centered cubic (bcc) $Ti_{38}V_{15}Nb_{23}Hf_{24}$ (*16*). Besides SRO and nanoprecipitates, a dual phase or lamellar structure can also play a notable role in manipulating the mechanical properties of HEAs, for instance, forming hexagonal close-packed (hcp)/fcc microstructures in $Fe_{50}Mn_{30}Co_{10}Cr_{10}$ (*17*)/$Cr_{20}Mn_6Fe_{34}Co_{34}Ni_6$ (*18*), recrystallized/nonrecrystallized microstructures in $Al_{0.1}$CoCrFeNi (*19*), or lamellar eutectic $AlCoCrFeNi_{2.1}$ (*20*).

Recently, Ren *et al.* (*21*) fabricated dual-phase nanolamellar HEAs of $AlCoCrFeNi_{2.1}$ by an additive-manufacturing route. They showed that these HEAs exhibit a combination of a high yield strength of ~1.3 GPa and a large uniform elongation of ~14%, which surpass those of other state-of-the-art additively manufactured metal/alloys. In the as-printed $AlCoCrFeNi_{2.1}$, a dual-phase nanolamellar structure consisting of alternating bcc and fcc nanolayers was observed, where the bcc lamellae were prominently rich in Al and Ni while the fcc lamellae were highly enriched by Co, Cr, and Fe. It was shown experimentally that, in Al_xCoCrFeNi HEAs, an fcc structure was more stable when $x < 0.5$ [~11–atomic % (at %) Al], fcc and bcc structures were of similar stability when $0.5 \leq x \leq 0.9$, and the bcc phase was more stable when $x > 0.9$ (~18–at % Al) (*22*).

By tuning Al concentration, Zhang *et al.* fabricated single-crystalline fcc CoCrFeNi (*23*) and bcc AlCoCrFeNi (*24*) HEA micropillars and nanopillars with typical orientations of [100], [110], and [111] experimentally. Both CoCrFeNi and AlCoCrFeNi HEAs demonstrated pronounced size effects on yield and flow stresses in three orientations under in situ uniaxial compression tests. Large-scale atomistic simulations revealed that dislocation slip, reaction, tangling and accumulation, and deformation twinning were responsible for the experimentally observed size effects on yield and flow stresses.

The tunable phase stability of these HEAs with varying Al concentrations (*22*) along with the nanolamellar structure (*21*) raise several interesting and yet important questions. What are the deformation mechanisms in the nanolamellar HEAs with alternating low and high Al concentrations? Are there differences in the phase stability and dislocation activity between low–Al concentration

[1]Materials Genome Institute, Shanghai University, Shanghai 200444, China. [2]Institute of High Performance Computing (IHPC), Agency for Science, Technology and Research (A*STAR), 1 Fusionopolis Way, #16-16 Connexis, Singapore 138632, Republic of Singapore. [3]Department of Materials Science and Engineering, City University of Hong Kong, Hong Kong SAR, China. [4]Department of Materials Science and Engineering, University of North Texas, Denton, TX 76207, USA. [5]Department of Mechanical Engineering, The University of Hong Kong, Hong Kong SAR, China. [6]Department of Materials Science and Engineering, The University of Tennessee, Knoxville, TN 37996, USA.
*Corresponding author. Email: srol@hku.hk (D.J.S.); pliaw@utk.edu (P.K.L.); zhangyw@ihpc.a-star.edu.sg (Y.-W.Z.)
†These authors contributed equally to this work.

and high–Al concentration lamellae? What are the effects of lamella thickness and crystalline orientation on their deformation mechanisms and mechanical properties? What is their mechanical performance, as compared with homogeneous HEAs? Clearly, answers to these critical questions not only are of importance for the in-depth understanding of deformation mechanisms and mechanical properties of HEAs with nanolamellar structures but also provide useful guideline for their rational design. This is the motivation for the current study.

Atomistic simulations not only can capture the structural features of nanolamellar HEAs but also reveal the deformation mechanisms in detail. Thereinto, molecular dynamic (MD) simulations (*23*–*26*) can access to longer-time and larger-size scales, as compared with density functional theory (DFT) calculations (*27*, *28*). For example, Li *et al.* (*25*) used MD simulations to study a nanocrystalline $Al_{0.3}CoCu_{0.7}FeNi$ HEA, whose grain sizes were comparable to those in experiments of Fu *et al.* (*29*). Their MD results (*25*) showed that the high strength in the nanocrystalline HEA without the sacrifice of ductility obtained in experiments (*29*) was attributed to the strain-induced fcc-to-bcc phase transformation. Therefore, here, we also use atomic-scale simulations and analyses to answer the above questions.

Here, we explore the deformation mechanisms and mechanical/functional properties of both homogeneous and nanolamellar Al_xCoCuFeNi HEAs using MD and DFT calculations. DFT calculations are performed to validate the interatomic potential, while MD simulations are used to simulate tensile deformation. Different simulation models are constructed to study the effects of the lamella geometry, elemental concentration, and loading direction on the mechanical response of the HEAs during tensile loading and then unloading. Deformation mechanisms in terms of phase transformations and dislocation activities are analyzed. The present work aims to gain an in-depth understanding in the composition-structure-property relations of nanolamellar HEAs and provide guidelines for the rational design of HEAs to achieve their novel mechanical and functional properties.

RESULTS

Validation of interatomic potential

It is well recognized that interatomic potentials play a pivotal role in MD simulations. Before presenting simulation results, we would like first to validate the interatomic potential used in the present work. Here, the embedded-atom method (EAM) potential of Zhou *et al.* (*30*) is used for MD simulations. This potential has reasonably reproduced the stacking fault energy (*25*), phase stability (*31*), and deformation mechanisms (*25*, *31*) of the experimental results (*22*, *29*, *32*–*34*) of the AlCoCuFeNi HEAs. We further examine the cohesive energies for 10 binary combinations of {Al, Co, Cu, Fe, and Ni} in the AB_3 $L1_2$ intermetallic crystal structure and five single elements of {Al, Co, Cu, Fe, and Ni} in the fcc crystal structure. The cohesive energies determined from the interatomic potentials used in the MD and from DFT are listed in table S1 (A and B). While the MD interatomic potential-based cohesive energies do not demonstrate perfect agreement with DFT calculations (as expected), they are remarkably successful in reproducing the important trends. For example, both results indicate that XAl_3 and XCu_3 (X = Al, Co, Cu, Fe, or Ni) exhibit higher cohesive energies (marked in red in table S1), and XCo_3, XFe_3, and XNi_3 (X = Al, Co, Cu, Fe, or Ni) have lower cohesive energies (marked in green in table S1). These trends indicate that the interatomic potential is able to capture the relative stabilities of local structures with different atomic environments.

Plastic-deformation behavior of homogeneous HEAs

For the easy comparison and discussion of the plastic-deformation behavior of nanolamellar HEAs, we first perform MD simulations on homogeneous Al_xCoCuFeNi HEAs to investigate their plastic-deformation behavior. The Al_xCoCuFeNi HEA simulation model is constructed by orienting an fcc box with [100], [010], and [001] directions aligned, respectively, along *x*, *y*, and *z* axes (Fig. 1A). The sizes of the homogeneous HEA model are set as $L = W = H = 17.28$ nm, and the elemental concentration of Al in the box (C) is set at 5, 7, 9, 11, 13, and 15 at % (Fig. 1B). The MD simulations are performed at a strain rate of 5×10^8 s^{-1} and a temperature of 300 K. The stress versus strain curves of the homogeneous HEAs loaded along the [001] direction, that is, *z* axis, are shown in fig. S1A. The phase profile and dislocation activity are presented in the fig. S1 (B to D) for $C = 5$ at % and fig. S1 (E to G) for $C = 15$ at %. From the stress versus strain curves, it is seen that after the stresses reach the ultimate tensile strength (UTS), a large majority of atoms in the $C = 5$–at % sample are still in the fcc phase while only a tiny fraction of atoms is in either the bcc phase or unknown lattice (fig. S1B). After the UTS (3.0 GPa), there is a small fraction of atoms transforming into the bcc phase and unknown lattice (fig. S1C), and there is no dislocation activity, as presented in fig. S1D. With

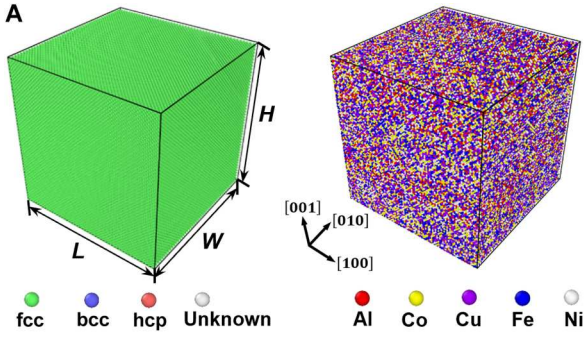

B

Case	Dimension	Concentration
1	$L = W = H$ = 17.28 nm	C = 5 at %
2		C = 7 at %
3		C = 9 at %
4		C = 11 at %
5		C = 13 at %
6		C = 15 at %

Fig. 1. Simulation model of the homogeneous HEAs. (**A**) Atomic configurations colored according to phase structure and element types. (**B**) Dimension ($L = W = H$) and Al concentration (C) used in the homogeneous HEA model.

increasing the Al concentration, the fractions of atoms in the bcc phase and unknown lattice increase, as exhibited in fig. S1 (E and F) for the C = 15–at % sample. Edge, screw, and mixed dislocations are observed after UTS (2.3 GPa) at the 15–at % sample. Hence, all the homogeneous HEAs exhibit a drastic softening behavior after the UTS due to the fcc-to-bcc transition and dislocation activities (for high–Al concentration samples), and the higher the Al concentration, the stronger the softening. This trend is consistent with the previous experimental study (*22*) that a lower Al concentration favors the fcc phase while a higher Al concentration favors the bcc phase.

Plastic-deformation behavior of nanolamellar HEAs

For nanolamellar HEAs, the simulation box is cut into four nanolayers (denoted as first, second, third, and fourth layers from the bottom, as presented in Fig. 2A). In all the model settings, the thickness and elemental concentration of the first and third layers are identical (h_1 and c_1), and those of the second and fourth layers are also identical (h_2 and c_2). To study the effect of the lamella geometry and composition on the mechanical response, we have selected the following geometric and compositional settings: (i) Geometry effect: Four cases of nanolamellar HEAs without a difference between h_1 and h_2, i.e., $h_1 = h_2$ = 4.32, 5.4, 6.48, and 7.56 nm, and c_1 = 5 at %, c_2 = 15 at % (see Fig. 2B). (ii) Geometry effect: Four cases of nanolamellar HEAs with a difference between h_1 and h_2, and $h_1 + h_2$ = 8.64 nm, i.e., (h_1 = 2.16 nm, h_2 = 6.48 nm), (h_1 = 2.88 nm, h_2 = 5.76 nm), (h_1 = 5.76 nm, h_2 = 2.88 nm), (h_1 = 6.48 nm, h_2 = 2.16 nm), and c_1 = 5 at %, c_2 = 15 at % (see Fig. 2C). (iii) Compositional effect: Four cases of nanolamellar HEAs with $h_1 = h_2$ = 4.32 nm, c_1 = 5 at %, c_2 = 10, 12, 17, and 20 at % (see Fig. 2D). The variation of elemental concentration in each atomic layers with position along thickness direction for the nanolamellar HEA with $h_1 = h_2$ = 4.32 nm, c_1 = 5 at %, and c_2 = 15 at % is calculated (fig. S2). Clearly, the elemental concentrations in each atomic layers are within reasonable range, i.e., ±1 at % for low Al concentration (5 at %), ±2 at % for high Al concentration (15 at %) and other elemental (Co, Cu, Fe, and Ni) concentrations (23.75 or 21.75 at %).

Uniaxial tensile-deformation simulations are performed on the nanolamellar HEAs loaded along the [001] direction (z axis) with the same strain rate and temperature as the homogeneous HEAs, and the stress-strain curves are shown in Fig. 3A. The stresses of all the HEAs increase monotonically with strain before UTS (from 0 to 0.04 strain). However, the nanolamellar HEAs ($h_1 = h_2$ = 4.32 nm to 7.56 nm, c_1 = 5 at %, and c_2 = 15 at %) demonstrate an ideal plastic-behavior posterior to UTS, i.e., there is a plateau for the stress from the 0.045 to 0.065 strain, which is clearly not observed in the homogeneous HEAs (i.e., C = 5 to 15 at % in Fig. 3A and fig. S1). The atomic configurations of the h_1 = 4.32-nm sample at a 0.045 strain colored by a phase structure according to the common neighbor analysis (CNA) (*35*) and a 0.05 strain colored by the dislocation structure according to the dislocation extraction analysis (DXA) (*36*) in Open Visualization Tool (OVITO) (*37*) are drawn in Fig. 3 (B and C, respectively). Clearly, the phase transformation from the fcc to bcc structure is the dominated deformation mechanism (see Fig. 3B). In addition, the phase transformation from fcc to an unknown structure also occurs mostly near the formed bcc structure, while no hcp structure is observed. Besides, a small number of dislocations with edge, screw, and mixed characters that can nucleate and propagate only in a limited distance (blocked) are also observed (Fig. 3C). These deformation mechanisms are seemingly similar to those observed in the homogeneous samples.

We have also analyzed the variation of fcc/bcc structure fraction and dislocation density with strain in the nanolamellar HEA with $h_1 = h_2$ = 4.32 nm, c_1 = 5 at % and c_2 = 15 at % during loading (see fig. S3A). This trend indicates that the phase transformation from the fcc to bcc structure occurs at ~0.04 strain, subsequently followed by

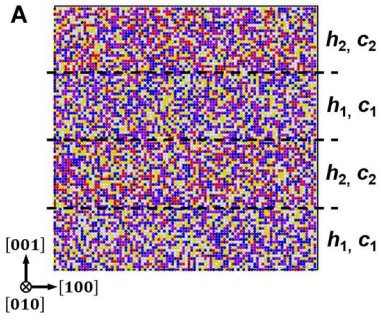

B

Case	Dimension	Concentration
7	$h_1 = h_2$ = 4.32 nm	c_1 = 5 at %, c_2 = 15 at %
8	$h_1 = h_2$ = 5.4 nm	
9	$h_1 = h_2$ = 6.48 nm	
10	$h_1 = h_2$ = 7.56 nm	

C

Case	Dimension ($h_1 + h_2$ = 8.64 nm)	Concentration
11	h_1 = 2.16 nm	c_1 = 5 at %, c_2 = 15 at %
12	h_1 = 2.88 nm	
13	h_1 = 5.76 nm	
14	h_1 = 6.48 nm	

D

Case	Dimension	Concentration (c_1 = 5 at %)
15	$h_1 = h_2$ = 4.32 nm	c_2 = 10 at %
16		c_2 = 12 at %
17		c_2 = 17 at %
18		c_2 = 20 at %

Fig. 2. Simulation geometries and compositions of the nanolamellar HEAs. (**A**) Four-layer nanolamellar HEA model (cross-sectional view). (**B**) Varying the layer thickness with $h_1 = h_2$, and the Al concentrations fixed at c_1 = 5 at % and c_2 = 15 at %. (**C**) Varying both h_1 and h_2 with $h_1 + h_2$ = 8.64 nm, and the Al concentrations fixed at c_1 = 5 at % and c_2 = 15 at %. (**D**) Varying the Al concentration, c_2, while keeping c_1 and geometry fixed.

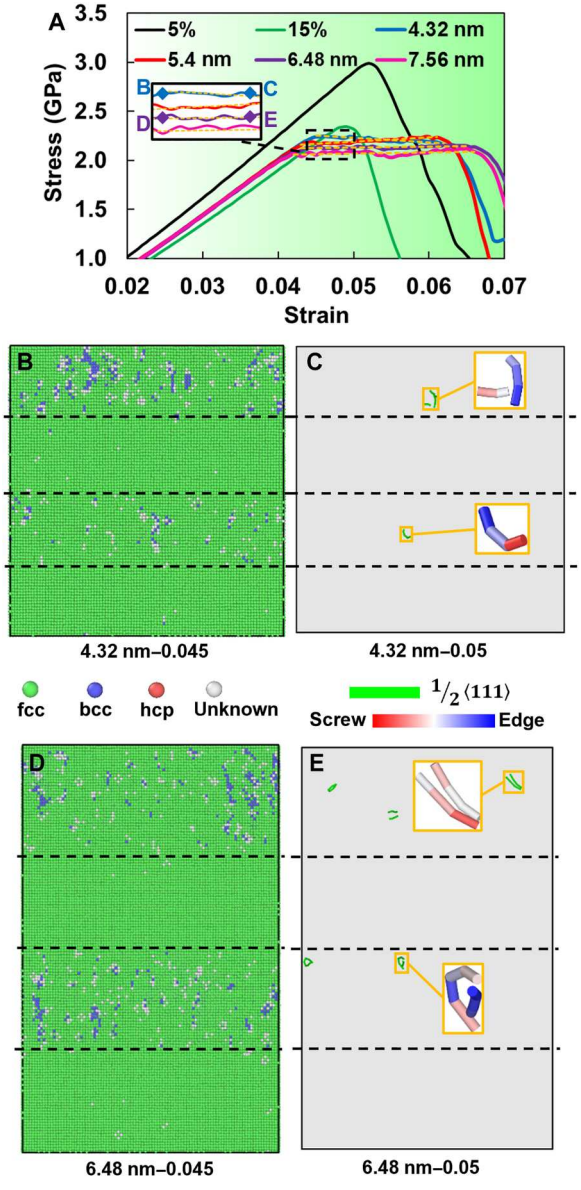

Fig. 3. Stress-strain curves and atomic configurations of the homogeneous and nanolamellar HEAs during uniaxial loading. (**A**) Variation of stress with strain for the homogeneous (C = 5 or 15 at %) and nanolamellar HEAs with h_1 = h_2 = 4.32 to 7.56 nm (c_1 = 5 at % and c_2 = 15 at %) during loading. Atomic configurations of the h_1 = 4.32-nm sample at strains of (**B**) 0.045 colored according to the phase structure and (**C**) 0.05 colored according to the dislocation structure, as indicated in (A). Atomic configurations of the h_1 = 6.48-nm sample at strains of (**D**) 0.045 colored according to the phase structure and (**E**) 0.05 colored according to the dislocation structure, as indicated in (A).

dislocation nucleation at a 0.05 strain, which is consistent with the observations in Fig. 3 (B and C) that phase transformation is coupled with dislocation nucleation. This nanolamellar HEA is also loaded along other two horizontal directions (fig. S4). The results demonstrate that the nanolamellar HEA does not exhibit ideal plasticity when loaded along horizontal directions. Phase transformations (fig. S4B) and dislocation nucleation/propagation occur in the whole HEA during loading (fig. S4C), which are similar to the homogeneous samples.

To gain an in-depth understanding for the peculiar ideal plasticity observed in the nanolamellar structure, we also examined the atomic configurations of the h_1 = 6.48-nm sample at strains of 0.045 and 0.05, and the results are shown in Fig. 3 (D and E, respectively). These results further confirm that the fcc-to-bcc phase transformation is the dominated deformation mechanism in the nanolamellar HEAs (Fig. 3, B and D), and the dislocations with edge, screw, and mixed characters are also present (Fig. 3, C and E). All the plastic activities, that is, phase transformations and dislocation nucleation/propagation, only occur in the second and fourth layers (i.e., high–Al concentration layers, 15 at %), while no plastic activities occur in the first and third layers (i.e., low–Al concentration layers, 5 at %). The plateau for the stress in the nanolamellar HEAs is ~2.1 to 2.2 GPa, which is close to the stress required for plastic activities in the high–Al concentration (15 at %) layer (2.3 GPa), but much lower than that in the low–Al concentration (5 at %) layer (3.0 GPa). Therefore, the high Al concentration facilitates the fcc-to-bcc phase transformation and dislocation nucleation/propagation, while the low Al concentration resists phase transformations and dislocation nucleation and blocks/confines phase transformation and dislocation propagations.

Effect of elemental concentration and lamella-thickness difference

To understand the deformation behavior of the nanolamellar HEAs, we further investigate the effect of elemental-concentration difference by changing c_2 from 10 to 20 at % (c_1 = 5 at %) on the mechanical response of nanolamellar HEAs (Fig. 4). It is seen that the elemental-concentration difference is able to change the duration and slope of the plateau. When the elemental-concentration difference is sufficiently large (c_2 = 17 to 20 at %, i.e., $|c_1 - c_2|/c_1$ = 240 to 300%), the nanolamellar HEAs exhibit similar deformation mechanisms (i.e., dominated by the fcc-to-bcc phase transformation along with dislocation nucleation/propagation in the first and third layers, as exhibited in Fig. 4 (D and E), and their stress-strain curves show a longer plateau with a positive slope, that is, a plastic-hardening behavior.

When c_2 = 10 at % (the elemental-concentration difference, $|c_1 - c_2|/c_1$ = 100%), the stress-strain curve (Fig. 4A) is similar to those of homogeneous HEAs, and the fcc-to-bcc phase transformation also occurs in the second and fourth layers at the stress peak (Fig. 4B). When c_2 = 12 to 15 at % (the elemental-concentration difference, $|c_1 - c_2|/c_1$ = 120 to 200%), the stress-strain curve (Fig. 4A) exhibits a shorter plateau with a negative slope, that is, a plastic-softening behavior.

These results clearly show that by tuning the composition difference of the layers, we are able to change the duration and slope of the plateau. These different behaviors can be understood by the fact that on the one hand, when the Al concentration is high, extensive plastic deformations due to the phase transformation and edge/screw/mixed dislocations will occur in the high–Al concentration layers, which tends to create a softening effect of the nanolamellar structure. On the other hand, these high activities of the phase transformation and dislocation nucleation and propagation will be confined and blocked by the low–Al concentration layers, which tends to create a strong hardening effect. Hence, it is the

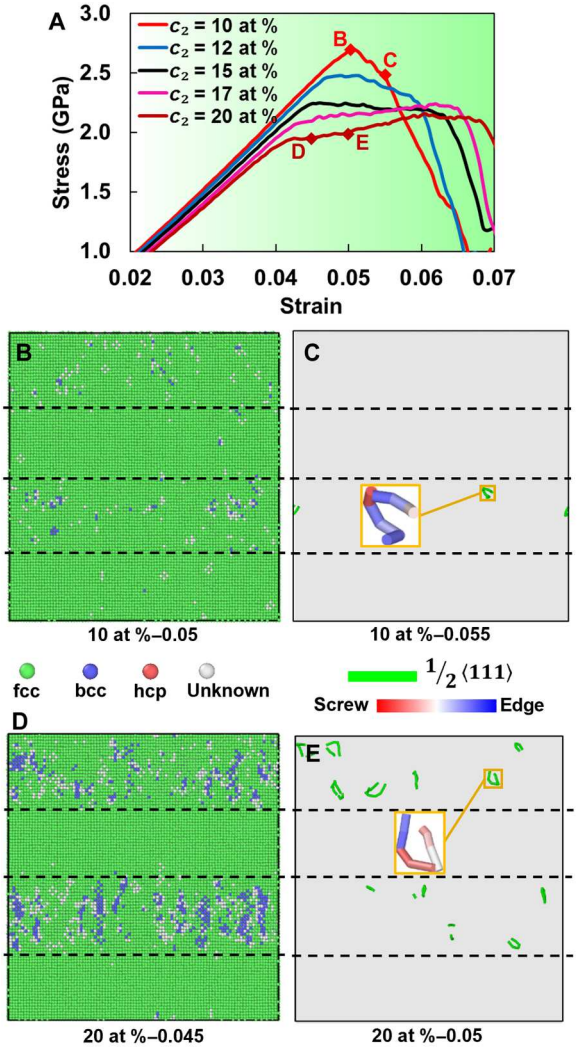

Fig. 4. Stress-strain curves and atomic configurations of the nanolamellar HEAs with c_1 = 5 at % and c_2 = 10 to 20 at %. (**A**) Variation of stress with strain for the nanolamellar HEAs with c_1 = 5 at % and c_2 = 10 to 20 at %. Atomic configurations of the c_2 = 10–at % sample at strains of (**B**) 0.05 colored according to the phase structure and (**C**) 0.055 colored according to the dislocation structure, as indicated in (A). Atomic configurations of the c_2 = 20–at % sample at strains of (**D**) 0.045 colored according to the phase structure and (**E**) 0.05 colored according to the dislocation structure, as indicated in (A).

competition of these two effects that gives rise to these different behaviors, that is, different plateau durations and slopes.

When Al concentration is higher than 20 at %, bcc phase is more stable than fcc phase (*31*). Nanolamellar HEA consisting of fcc lamellae with a low Al concentration (5 at %) and bcc lamellae with a much higher Al concentration (35 at %) is simulated (fig. S5). The results indicate that the nanolamellar HEA consisting of the fcc and bcc lamellae does not exhibit ideal plasticity. The underlying reason is that the interphase boundaries act as dislocation nuclei (fig. S5C), and the stress drops off once dislocations propagate into the low–Al concentration layers after nucleation at the interphase boundaries (fig. S5D).

We also explore the effect of the lamella-thickness difference by varying h_1 from 2.16 to 6.48 nm (h_1 + h_2 = 8.64 nm) on the mechanical response of nanolamellar HEAs (fig. S6). The results indicate that when the lamellar-thickness difference is not large (h_1 = 2.88 to 5.76 nm, h_2 = 5.76 to 2.88 nm, i.e., $|h_1 - h_2|/h_1 \leq 100\%$, and $|h_1 - h_2|/h_2 \leq 100\%$), the nanolamellar HEAs display similar deformation mechanisms (i.e., dominated by the fcc-to-bcc phase transformation along with the dislocation nucleation/propagation/confinement in the first and third layers) and stress-strain curves with plateaus (i.e., ideal plasticity) as those in Fig. 3. When the thickness of the low–Al concentration layer is small and that of the high–Al concentration layer is large, e.g., h_1 = 2.16 nm and h_2 = 6.48 nm ($|h_1 - h_2|/h_1 \geq 200\%$), the stress-strain curve has a long plateau with a negative slope. This is because the confinement and slip-blocking effects are weaker because of the small volume fraction of the low–Al concentration layers. Conversely, when the thickness of the low–Al concentration layer is large while that of the high–Al concentration layer is small, e.g., h_1 = 6.48 nm and h_2 = 2.16 nm ($|h_1 - h_2|/h_2 \geq 200\%$), the stress-strain curve has a short plateau with a positive slope. This trend is because of the stronger confinement and slip-blocking effects arising from the high-volume fraction of the low–Al concentration layers.

Directional phase transformation in nanolamellar HEAs

Thus far, we have shown that the dominated deformation mechanism in nanolammellar HEAs loaded along the [001] direction is the fcc-to-bcc phase transformation. We note that the strain-induced phase transformation is directional in the high–Al concentration layers (Fig. 5, A and B), mainly along the loading direction, that is, the [001] direction. To reveal the origin of this directional fcc-to-bcc phase transformation, we examine the densities of fcc-structured and bcc-structured HEAs during tensile deformation (Fig. 5C). Clearly, the densities of both fcc and bcc structures increase monotonically with strain during tensile deformation. Besides, the density of the fcc structure is always higher than that of the bcc phase, i.e., the volume of the fcc structure is always lower than that of the bcc phase for the same number of atoms. Therefore, the volume expansion tends to favor the bcc phase, thus facilitating the transformation from the (high-density) fcc to (low-density) bcc structure. Once there is a bcc nucleus (a blue ball in Fig. 5D), the regions at the top and bottom tips of the nucleus along the loading direction (green areas in Fig. 5D) undergo the maximum volume expansion. Hence, the fcc-to-bcc transformation at the top tip will propagate upwards and while that at the bottom tip will propagate downwards, causing the directional phase transformation.

We also investigate the effect of the tensile loading direction on the mechanical response of nanolamellar HEAs. Besides the [001] direction, another three loading directions, that is, along [111], [123], and [110], are also studied. The stress-strain curves and atomic configurations of the nanolamellar HEAs for h_1 = h_2 = 4.32 nm following these three loading directions are shown in figs. S7 and S8. It is seen that that there is no plateau in these three loading directions. The underlying origin is that for loading along these three directions, dislocation nucleation and propagation are the dominant deformation mechanism, and little phase transformation is observed. As a result, these dislocations are able to propagate across the different layers readily, which is quite different from that observed in the [001] loading direction, where the fcc-to-bcc phase transformation is the dominant deformation mechanism. Therefore, the unique ideal plastic behavior with the directional

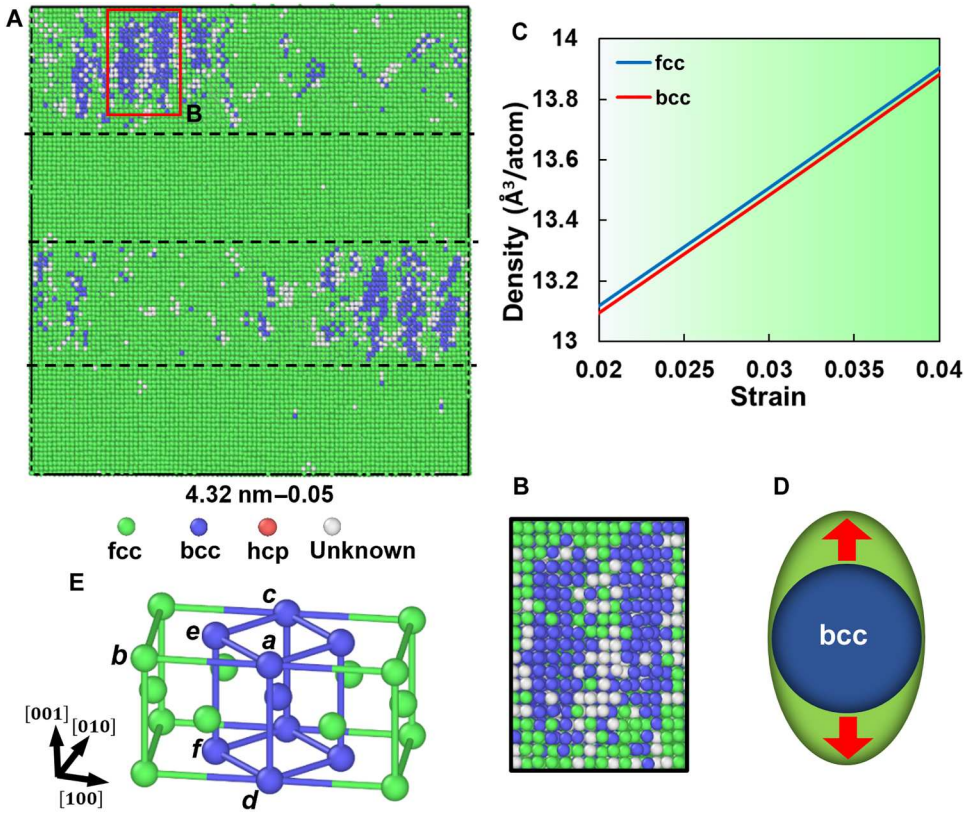

Fig. 5. Atomic configurations of the nanolamellar HEA, densities of fcc and bcc structures as a function of strain, schematic diagram of the structure under vertical tension, and schematic illustration of phase transformation. (**A**) Atomic configuration of the h_1 = 4.32-nm sample at a strain of 0.05 during loading with a local region drawn in (**B**). (**C**) Densities of fcc and bcc structures as a function of strain during tension. (**D**) Schematic diagram of the structure under vertical tension. (**E**) Schematic illustration of phase transformation from the fcc to bcc phase.

phase transformation in nanolamellar HEAs is strongly dependent on the loading direction.

We find that the directional phase transformation from the fcc to bcc structure follows the tetragonal deformation path, i.e., Bain path (*38*), as presented in Fig. 5E. In the original fcc lattice as shown in Fig. 5E, the length $ab = ac = ad$, while $ea = ec < ef$. When the fcc phase (a green-atom structure in Fig. 5E) is subjected to the lattice distortions and loading along the [001] direction of the HEAs, the length, *ef*, decreases, leading to the facile phase transformation from the fcc to bcc (a blue-atom structure in Fig. 5E) phase. This well-aligned fcc and bcc lattices in the [001] direction do not appear in [111], [123], and [110] directions. This preferential [001] direction in the occurrence of phase transformation has also been observed in the $Al_{0.25}CoCu_{0.75}FeNi$ (*25*). After the phase transformation, the phase boundaries between the remaining fcc and transformed bcc phases provide favorable nucleation sites for dislocations. On the one hand, phase transformation and dislocation nucleation and propagation cause the release of the stress level. On the other hand, the transformed bcc domains and the fcc-bcc phase boundaries can also block dislocation propagation and cause their limited mean free paths, thus increasing the stress level. It is the preferential phase transformation and dislocation nucleation/confinement that contribute to the unique ideal plastic behavior in the [001] direction.

Shape memory of nanolamellar HEAs

We further study the unloading behavior for the sample with c_1 = 5 at %, c_2 = 15 at %, $h_1 = h_2$ = 4.32 nm, and loading along the [001] direction. Stress-strain curves during loading and unloading under different strains are presented in Fig. 6A. With loading from a 0.04 strain, the sample undergoes elastic deformation (negligible phase transformation as presented in Fig. 6B). At the strain level from 0.04 to 0.06, the fcc-to-bcc phase transformation is the dominated deformation mechanism (Fig. 6, A to C) along with a small portion of dislocation nucleation/propagation/confinement (Fig. 6E). When unloading is performed on the sample before the sharp decrease of stress (Unloading-I, Unloading-II, and Unloading-III in Fig. 6A), i.e., elastic and ideal plastic (plateau) regimes, all the stress-strain curves almost return back to their origin, exhibiting fully reversed deformation (i.e., shape memory).

Local atomic configurations of the regions indicated in Fig. 6E are shown in Fig. 6 (G and H). These configurations indicate that the edge/screw/mixed dislocations nucleate at the fcc-bcc phase boundaries, subsequently propagate in the fcc phase, and lastly are blocked at neighboring fcc-bcc phase boundaries. Local atomic configurations of the region with dislocations during loading to a 0.064 strain and unloading to a 0.059 strain are presented in Fig. 6 (I and J, respectively). The structure changes between Fig. 6I and Fig. 6J indicate that the dislocation annihilation and phase transformation from the bcc to fcc phase occur during

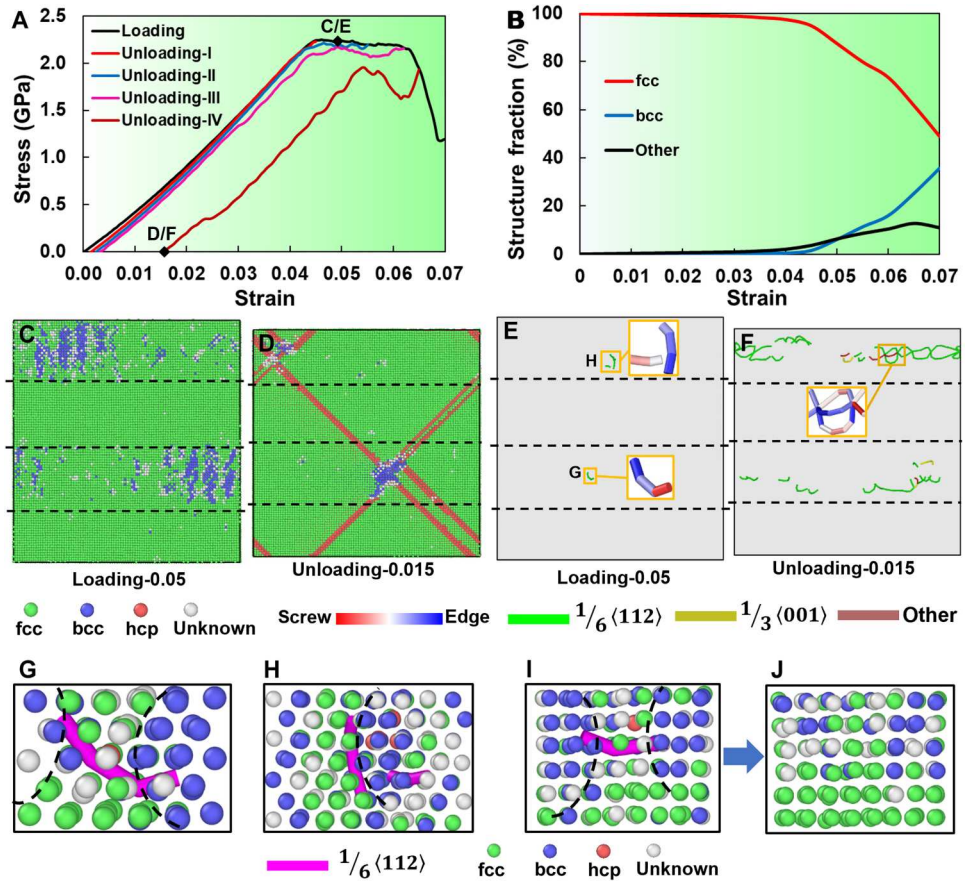

Fig. 6. Stress-strain curves, atomic fractions of different phase structures, and atomic configurations of the nanolamellar HEA during loading and unloading. (**A**) Variation of stress with strain for the nanolamellar HEA with $h_1 = h_2 = 4.32$ nm during loading and unloading. (**B**) Atomic fractions of different phase structures as a function of strain during loading. Atomic configurations of the $h_1 = 4.32$-nm sample at strains of (**C**) 0.05 during loading and (**D**) 0.015 during unloading colored according to the phase structure, and (**E**) 0.05 during loading and (**F**) 0.015 during unloading colored according to the dislocation structure, as indicated in (A). (**G** and **H**) Local atomic configurations colored according to the phase structure and dislocation structure of the regions indicated in (E). Local atomic configurations colored according to the phase structure and dislocation structure at (**I**) 0.064 strain and (**J**) 0.059 strain during unloading.

unloading in the samples before the sharp decrease of the stress (Unloading-I, Unloading-II, and Unloading-III in Fig. 6A), leading to the reversible plastic deformations and shape memory of nanolamellar HEAs. Variation of fcc/bcc structure fraction and dislocation density with strain during Unloading-II of the nanolamellar HEA with $h_1 = h_2 = 4.32$ nm, $c_1 = 5$ at %, and $c_2 = 15$ at % is analyzed (fig. S3B). The results indicate that the phase transformation from the bcc to fcc structure occurs together with the dislocation annihilation. However, when unloading is performed on the sample posterior to the plateau regime (Unloading-IV in Fig. 6A), the dislocation annihilation and phase transformation from the bcc to fcc phase partially occur along with new dislocation nucleation and propagation (Fig. 6, D and F), resulting in the residual strain of the nanolamellar HEAs.

DISCUSSION

Stability and fabrication of nanolamellar HEAs

It was reported experimentally that in $Al_xCoCrFeNi$ HEAs, an fcc structure was more stable when $x < 0.5$ [~11–at % Al], fcc and bcc structures were of similar stability when $0.5 \leq x \leq 0.9$ (from 11– to 18–at % Al) (*22*). We have also studied the phase stability of $Al_xCoCu_{1-x}FeNi$ ($x = 0.1$ to 0.9) HEAs with the interatomic potential used here. Our results indicate that the fcc phase was more stable when $x \leq 0.4$ (10–at % Al) and the fcc and bcc phases were of similar stability (the cohesive-energy difference is within 0.003 eV per atom) when $x = 0.6$ (15–at % Al) (*31*). Therefore, the interatomic potential is able to well reproduce the phase stability with different Al concentration. Besides, both the low–Al concentration (5 at %) layer and the high–Al concentration (15 at %) layer could stabilize in the fcc phase, supporting the construction of an initial model in the fcc phase.

Accumulative roll bonding (ARB) has been widely used to fabricate metallic nanolamella. For example, Ekiz *et al.* (*39*) fabricated nanolamellar Cu/Nb composites by ARB, leading to a nominal layer thickness of 18 nm. Carpenter *et al.* (*40*) fabricated nanolamellar Zr/Nb composites with 90-nm individual layers using ARB. Wei *et al.* (*41*) fabricated nanolamellar Cu/V composites with an average layer thickness of ~80 nm by ARB. It is expected that ARB could also be used to fabricate nanolamellar HEAs. Besides, additive manufacturing, e.g., the laser powder bed fusion, has been reported to produce nanolamellar $AlCoCrFeNi_{2.1}$ HEAs (*21*).

Comparisons with experiments

Nanolamellar metals/alloys often have a large number of interfaces because of the small lamella thicknesses. During the plastic deformation, edge/screw/mixed dislocations are emitted from one interface (e.g., domain boundary and phase boundary) segment and disappear at another interface segment promptly, leaving no or few dislocations to accumulate inside the grain interior (*42*). In general, the accumulation of dislocations contributes to work hardening, thus improving ductility. Dislocation accumulation becomes difficult in nanolamellar structures (*43*). Therefore, nanolamellar metals/alloys generally exhibit high strength but come at the expense of low ductility (*21*, *42*, *44*). Recently, Ren *et al.* (*21*) used the laser powder bed fusion to print fcc + bcc dual-phase nanolamellar $AlCoCrFeNi_{2.1}$ HEAs, where rapid solidification produced a high density of pre-existing dislocations. Besides, the alternating fcc and bcc nanolamellae have semicoherent interfaces, which can impose strong mutual confinement on the dislocation glide (*45*, *46*). Therefore, these nanolamellar HEAs exhibit a combination of a high yield strength of ~1.3 GPa and a large uniform elongation of ~14%, owing to the high work-hardening capability.

Cantor *et al.* (*47*) used melt-back technique to grow Al-Al_2Cu lamellar structures, showing semicircular dislocation segments concentrated at the lamellar interfaces. This trend indicates that the deformation of Al-Al_2Cu lamellar structures is dominated by the differential thermal contraction stresses at the lamellar interfaces during manufacture. The thermal expansion coefficient of Al_2Cu increases with temperature, which is $TE_1 = 5.92 \times 10^{-5}\ K^{-1}$ at room temperature (*48*). The thermal expansion coefficient of Al at room temperature is $TE_2 = 2.34 \times 10^{-5}\ K^{-1}$ (*49*), whose difference is $w\% = |(TE_1 - TE_2)/TE_1| = 60.5\%$, as compared with that of Al_2Cu (*48*). The huge difference in thermal expansion coefficients between Al and Al_2Cu leads to the differential thermal contraction stresses at the lamellar interfaces of Al-Al_2Cu lamellar structures, resulting in the concentration of dislocations at the interfaces. We have also performed simulations on the thermal expansion of the low–Al concentration (5 at %) and high–Al concentration (15 at %) HEAs. The variations of their lattice constants with temperature are shown in fig. S9, where their thermal expansion coefficients are $TE_3 = 2.02 \times 10^{-5}\ K^{-1}$ (5 at %) and $1.88 \times 10^{-5}\ K^{-1}$ (15 at %), respectively. The difference in thermal expansion coefficient between the low–Al concentration and high–Al concentration layers is $w\% = |(TE_3 - TE_4)/TE_3| = 6.9\%$, which is much lower than that of Al_2Cu and Al (60.5%). Therefore, differential thermal contraction stresses at the lamellar interfaces are not dominated in our nanolamellar $Al_xCoCuFeNi$ HEAs during deformation. Instead, the phase transformation coupled with dislocation nucleation and propagation is dominated in the high–Al concentration layers along with the confinement and slip-blocking effect in the low–Al concentration layers.

Our $Al_xCoCuFeNi$ HEAs consist of fcc lamellae with a low Al concentration (the fcc phase is stable under strain) and a high Al concentration (the fcc phase is metastable and tends to transform to a bcc structure under strain). With a proper choice of the geometry, composition, and loading direction, these $Al_xCoCuFeNi$ nanolamellar HEAs can exhibit ideal plastic, hardening, or softening behavior. In the present study, the phase transformations and dislocation nucleation/propagation in the high–Al concentration layers provide the plastic deformation and ductility, while the confinement and blockage of these plastic activities by the low–Al concentration layers provide the strengthening, which is to some extent similar to and yet different from the work hardening of dual-phase nanolamellar $AlCoCrFeNi_{2.1}$ HEAs (*21*). It is noted that our nanolamellae have coherent interfaces, which do not easily emit/absorb dislocations. Instead, edge/screw/mixed dislocations nucleate at the fcc-bcc phase boundaries, and the glide is confined by the low–Al concentration layers inside the nanolamellae. The competition between these continuous phase transformations and the emission and propagation of dislocations in the high–Al concentration layers and the confinement and blockage of these plastic activities by the low–Al concentration layers lead to the hardening, ideal plastic, and softening behavior of the nanolamellar HEA structures. Besides, these dislocation activities and phase transformations are reversible because of the small length scale, leading to their reversible behavior and shape memory. The present study clearly demonstrates an interesting pathway for the manipulation of HEAs at the nanoscale level that leads to the strength-ductility synergy and functionality.

Local atomic configurations

In HEAs, each atom is surrounded by distributions of different types of atoms. Considering each atom has n_1 first near neighbors, the cluster of each atom together with its n_1 first near neighbors consists of $n_1 + 1$ atoms. The number of different local atomic configurations, N_1, of $n_1 + 1$ atoms in a multicomponent alloy with c components is (*11*)

$$N_1 = c^{n_1+1} \tag{1}$$

Studying the vast number of local atomic configurations in alloys poses a notable challenge in materials science. In the case of HEAs, this complexity is particularly pronounced. For example, for equimolar fcc AlCoCuFeNi HEA, $c = 5$ and $n_1 = 12$; hence, $N_1 = 5^{13} = 1.2 \times 10^9$. The number of potential atomic configurations in the alloy reaches the order of trillions, making it virtually impossible to explore the entire range of structures using current modeling methods alone.

Various strategies have been explored to tackle this challenge. One approach is to use representative subsets of atomic configurations to gain valuable insights into the properties and behavior of alloys (*23*–*28*). Although this approach does not encompass the complete parameter space, it allows for the study of a diverse range of configurations while managing the computational complexity involved. The selection of the subsets typically involves statistical sampling, or informed selection strategies, ensuring a meaningful and representative sampling. However, it is essential to acknowledge the limitations of the modeling methods commonly used in alloy research. The widely used special quasi-random structure (SQS) model (*27*), for instance, can only consider systems with hundreds of atoms because of computational constraints. This limitation prevents a comprehensive exploration of larger atomic ensembles. Similarly, all-atom–based methods, while providing a detailed representation of individual atoms, suffer from the same limitation of computational cost and system size.

Nonetheless, despite these limitations, the insights gained from studying representative subsets of atomic configurations are valuable. By capturing essential trends and phenomena within the explored configurations, researchers have made substantial contributions to our understanding of alloy behavior, such as

mechanical properties (*23*, *24*), phase transformations (*25*), and electronic structures (*27*, *28*). It is important to note that experimental characterization techniques play a crucial role in validating and complementing the findings from modeling studies. To advance the field further, researchers are actively exploring alternative strategies. For instance, a multiscale approach that combines different modeling techniques and integrates experimental data can provide a more comprehensive understanding of HEAs.

While the number of local atomic configurations in alloys, especially HEAs, is vast and current modeling methods have limitations in exploring the entire range of structures, researchers use representative subsets to gain valuable insights into alloy properties and behavior. We have also performed simulations with additional representative subsets, i.e., different random number to generate different initial elemental distributions (fig. S10, A to C). Variation of stress with strain during loading for nanolamellar HEAs with different random numbers is shown in fig. S10D. Clearly, all of them exhibit similar stress-strain curves during loading, demonstrating ideal plasticity. This trend indicates that our representative subsets are robust. It is crucial to acknowledge the limitations of the SQS model and all-atom–based methods, which stem primarily from computational constraints and restricted system sizes. However, ongoing research efforts, including the development of alternative strategies and multiscale approaches, are continuing to expand our understanding of alloys and bridge the gap between modeling and experiment.

Strategy to design HEAs with superior mechanical and functional properties

The present work indicates that the introduction of nanolamellae in HEAs with structural heterogeneities can achieve novel mechanical (ideal plasticity) and functional (shape memory) properties. Figure 7 provides a schematic illustration of the proposed HEA-design strategy for superior mechanical and functional properties via nanolamellae. The central point is that the elemental concentration can produce a pseudocomposite microstructure of fcc-stable and fcc-metastable (transform to bcc under strain) nanolamellae. Using the five elements, labeled I, II, III, IV, and V, as shown in Fig. 7A as an example, we illustrate the design strategy to form such a composite microstructure. First, all five elements tend to form a stable fcc structure in the random solid-solution phase; second, by tuning the elemental concentration (e.g., low I and high I concentrations), the low–I concentration lamella is a stable fcc phase (Fig. 7B), while the high–I concentration lamella is a metastable fcc (transform to a bcc phase under strain) (Fig. 7C); last, we are able to design nanolamellar HEAs with a pseudocomposite microstructure consisting of fcc-stable and fcc-metastable nanolamellae with a tunable nanolamella thickness, thickness ratio, and elemental-concentration difference (Fig. 7D). Such an HEA tends to produce an fcc-to-bcc phase transformation coupled with the dislocation nucleation, propagation in fcc-metastable nanolamellae, and confinement and blockage of these plastic activities by the fcc-stable nanolamellae under loading, and the dislocation activities and phase transformations are reversible because of the small length scale during unloading, thus leading to a pseudocomposite microstructure with both the ideal plasticity and shape memory.

In summary, we performed MD and DFT calculations to investigate the composition-structure-property relations of Al_xCoCuFeNi HEAs. Our DFT calculations demonstrate that the interatomic potential used in the MD simulations captures the relative stabilities of the local structures in different atomic environments. The MD simulations demonstrate that the nanolamellar HEAs loaded along the [001] direction exhibit ideal plastic behavior during uniaxial tensile loading, a feature not observed in the homogeneous HEAs. The unique deformation mechanisms of phase transformation coupled with edge/screw/mixed dislocation nucleation and propagation in the high–Al concentration layers, and the confinement and blockage by the low–Al concentration layers lead to the ideal plasticity in nanolamellar HEAs. During unloading, dislocation annihilation and reverse phase transformation occur in the nanolamellar structures before the marked decrease of strain at loading, exhibiting shape memory. We also showed that the lamella geometry, phase composition, and loading direction affect the ideal plastic behavior and shape memory. The present study not only reveals the role of elemental concentration and nanolamellar structure in governing the phase transformation and dislocation activity in HEAs but also provides guidelines for the rational design of HEAs with high-performance mechanical and functional properties.

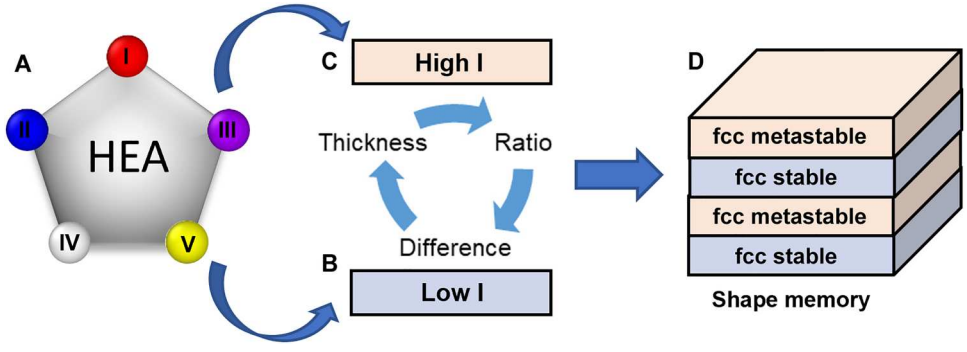

Fig. 7. Schematic diagram illustrating the strategy to design nanolamellar HEAs with ideal plasticity and shape memory. (**A**) Design of a HEA with five elements (I, II, III, IV, and V). Formations of (**B**) low concentration of the element I (an fcc phase) and (**C**) high concentration of element I (a metastable fcc). (**D**) Construction of nanolamellar HEAs with ideal plasticity and shape memory via a tunable nanolamella thickness, thickness ratio, and elemental-concentration difference.

MATERIALS AND METHODS

Atomic potential

A large-scale atomic/molecular massively parallel simulator (LAMMPS) package (*50*) with the EAM potential of Zhou *et al.* (*30*) is used for MD simulations. This potential has reproduced key aspects of the experimental mechanical-testing results of the AlCoCuFeNi HEAs. For example, with this potential, Li *et al.* (*25*) revealed the origin for high strength without sacrificing the ductility of $Al_{0.25}CoCu_{0.75}FeNi$ HEA in the experiment (*29*). The intrinsic stacking fault computed by MD simulations (*25*) is 25.6 ± 4.6 mJ/m^2, which is consistent with previous experimental results of 19.7 to 49 mJ/m^2 for similar HEAs (*32*–*34*). We also used this potential to study the phase stability of $Al_xCoCu_{1-x}FeNi$ (x = 0.1 to 0.9) HEAs (the fcc phase is more stable when $x \leq 0.4$, but the bcc phase is more stable when $x > 0.4$) and deformation mechanisms of the fcc structure (the phase transformation is dominated) and the bcc structure (the dislocation activity is dominated) (*31*), which are consistent with experimental measurements (*22*, *29*). We have further checked the cohesive energies of atomic pairs in the crystal structure (table S1). A good agreement in the stacking fault energy, phase stability, deformation mechanism, and cohesive energy validates the reliability of the atomic potential used in the study.

Cohesive energy

DFT calculations and MD simulations were performed to determine the cohesive energies of binary $L1_2$ alloys for all A-B elemental pairs and fcc crystal structures for single elements (A) in {Co, Cu, Fe, Ni, and Al}. A Vienna Ab initio Simulation Package (VASP) (*51*) with a plane-wave basis and projector augmented wave potentials (*52*, *53*) was used for DFT calculations. The Perdew, Burke, and Ernzerhof exchange correlation energy functional within the generalized gradient approximation was used (*54*). For the AB_3 binary $L1_2$ alloys, the cohesive energy is

$$E_c(AB_3) = -\frac{1}{4}[E_g(A) + 3E_g(B) - E_b(AB_3)] \quad (2)$$

where $E_b(AB_3)$ is the energy of the fully relaxed AB_3 structure, and $E_g(A)$ and $E_g(B)$ are the energies of isolated A and B atoms in their ground states, respectively. For the single-element fcc crystal structure, the cohesive energy is

$$E_c(A) = -\frac{1}{4}[4E_g(A) - E_b(A)] \quad (3)$$

where $E_b(A)$ is the energy of the fully relaxed fcc crystal structure consisting of the element A.

To compute the ground-state energies of the symmetry-broken spin-polarized magnetic ground state of an isolated atom, DFT calculations were performed for a single atom in a large cubic cell ($14 \times 14 \times 14$ Å^3) with periodic boundary conditions to avoid interactions with its periodic images. Relaxation runs were done by performing spin-polarized calculations and by allowing the ionic positions, cell volume, and cell shape to relax. The convergence tolerance for the electronic self-consistency was set at 10^{-8} eV, and the plane-wave energy cutoff was 800 eV. The bulk energies of the AB_3 $L1_2$ alloy were calculated by fully relaxing the ion positions and periodic-cell lattice parameters to electronic self-consistency with a tolerance of 10^{-8} eV and a force convergence tolerance of 10^{-4} eV/Å. A plane-wave energy cutoff of 520 eV and k point mesh of a $15 \times 15 \times 15$ per cell were applied for all calculations.

Model construction

The lattice constant of the fcc $Al_xCoCuFeNi$ was initially set at 3.6 Å in a simulation cell containing 442,368 atoms (17.28 nm by 17.28 nm by 17.28 nm). Four tensile-loading directions along [001], [110], [123], and [111] directions are simulated. For the [001] case, the box is oriented with [100], [010], and [001] directions aligned, respectively, with x, y, and z axes. For the [110] case, the box is oriented with [001], [1$\bar{1}$0], and [110] directions aligned, respectively, with x, y, and z axes. For the [123] case, the box is oriented with [1$\bar{2}$1], [41$\bar{2}$], and [123] directions aligned, respectively, with x, y, and z axes. For the [111] case, the box is oriented with [11$\bar{2}$], [$\bar{1}$10], and [111] directions aligned, respectively, with x, y, and z axes. The initial sample was constructed by populating atomic sites randomly with Al, Co, Cu, Fe, and Ni subject to the desired elemental compositions in each lamella for nanolamellar HEAs or in the whole box for homogeneous HEAs.

Tensile deformation

Before applying tensile deformation, the HEAs were thermally equilibrated at 300 K for 0.03 ns with the integration time step of 1 fs, via MD simulations in an isothermal-isobaric (NPT) ensemble (zero stress in all three directions). Uniaxial tensile loading was applied in the z direction at a strain rate of 5×10^8 s^{-1} for 0.2 ns at 300 K. Strain rates of 5×10^8 s^{-1} have been achieved, e.g., under laser shocking (*55*, *56*). After that, unloading was performed for the samples under different strains. During deformation, the NPT ensemble was used in the x and y directions to maintain a zero-lateral pressure (i.e., a constant uniaxial strain rate). Periodic boundary conditions were applied in all three directions. OVITO (*37*) was used to visualize atomic configurations and analyze simulation results by identifying phase structures (CNA) (*35*) and dislocation structures (DXA) (*36*).

Supplementary Materials

This PDF file includes:

Figs. S1 to S10
Table S1
Legend for data S1

Other Supplementary Material for this manuscript includes the following:

Data S1

REFERENCES AND NOTES

1. W. Sun, Y. Zhu, R. Marceau, L. Wang, Q. Zhang, X. Gao, C. Hutchinson, Precipitation strengthening of aluminum alloys by room-temperature cyclic plasticity. *Science* **363**, 972–975 (2019).
2. J. Sato, T. Omori, K. Oikawa, I. Ohnuma, R. Kainuma, K. Ishida, Cobalt-base high-temperature alloys. *Science* **312**, 90–91 (2006).
3. Z. Zhang, Z. Yang, S. Lu, A. Harte, R. Morana, M. Preuss, Strain localisation and failure at twin-boundary complexions in nickel-based superalloys. *Nat. Commun.* **11**, 4890 (2020).
4. J.-W. Yeh, S.-K. Chen, S.-J. Lin, J.-Y. Gan, T.-S. Chin, T.-T. Shun, C.-H. Tsau, S.-Y. Chang, Nanostructured high-entropy alloys with multiple principal elements: Novel alloy design concepts and outcomes. *Adv. Eng. Mater.* **6**, 299–303 (2004).
5. B. Cantor, I. T. H. Chang, P. Knight, A. J. B. Vincent, Microstructural development in equiatomic multicomponent alloys. *Mater. Sci. Eng. A* **375**, 213–218 (2004).
6. B. Gludovatz, A. Hohenwarter, D. Catoor, E. H. Chang, E. P. George, R. O. Ritchie, A fracture-resistant high-entropy alloy for cryogenic applications. *Science* **345**, 1153–1158 (2014).

7. Z. Lei, Y. Wu, J. He, X. Liu, H. Wang, S. Jiang, L. Gu, Q. Zhang, B. Gault, D. Raabe, Z. Lu, Snoek-type damping performance in strong and ductile high-entropy alloys. *Sci. Adv.* **6**, eaba7802 (2020).
8. C. Lee, G. Kim, Y. Chou, B. L. Musicó, M. C. Gao, K. An, G. Song, Y.-C. Chou, V. Keppens, W. Chen, P. K. Liaw, Temperature dependence of elastic and plastic deformation behavior of a refractory high-entropy alloy. *Sci. Adv.* **6**, eaaz4748 (2020).
9. Y. Zhang, T. T. Zuo, Z. Tang, M. C. Gao, K. A. Dahmen, P. K. Liaw, Z. P. Lu, Microstructures and properties of high-entropy alloys. *Prog. Mater. Sci.* **61**, 1–93 (2014).
10. S. Chen, Z. H. Aitken, S. Pattamatta, Z. Wu, Z. G. Yu, D. J. Srolovitz, P. K. Liaw, Y.-W. Zhang, Short-range ordering alters the dislocation nucleation and propagation in refractory high-entropy alloys. *Mater. Today* **65**, 14–25 (2023).
11. B. Cantor, Multicomponent high-entropy Cantor alloys. *Prog. Mater. Sci.* **120**, 100754 (2021).
12. Q. Ding, Y. Zhang, X. Chen, X. Fu, D. Chen, S. Chen, L. Gu, F. Wei, H. Bei, Y. Gao, M. Wen, J. Li, Z. Zhang, T. Zhu, R. O. Ritchie, Q. Yu, Tuning element distribution, structure and properties by composition in high-entropy alloys. *Nature* **574**, 223–227 (2019).
13. S. Chen, Z. H. Aitken, S. Pattamatta, Z. Wu, Z. G. Yu, D. J. Srolovitz, P. K. Liaw, Y.-W. Zhang, Simultaneously enhancing the ultimate strength and ductility of high-entropy alloys via short-range ordering. *Nat. Commun.* **12**, 4953 (2021).
14. T. Yang, Y. L. Zhao, Y. Tong, Z. B. Jiao, J. Wei, J. X. Cai, X. D. Han, D. Chen, A. Hu, J. J. Kai, K. Lu, Y. Liu, C. T. Liu, Multicomponent intermetallic nanoparticles and superb mechanical behaviors of complex alloys. *Science* **362**, 933–937 (2018).
15. Z. Fu, L. Jiang, J. L. Wardini, B. E. MacDonald, H. Wen, W. Xiong, D. Zhang, Y. Zhou, T. J. Rupert, W. Chen, E. J. Lavernia, A high-entropy alloy with hierarchical nanoprecipitates and ultrahigh strength. *Sci. Adv.* **4**, eaat8712 (2018).
16. S. Wei, S. J. Kim, J. Kang, Y. Zhang, Y. Zhang, T. Furuhara, E. S. Park, C. C. Tasan, Natural-mixing guided design of refractory high-entropy alloys with as-cast tensile ductility. *Nat. Mater.* **19**, 1175–1181 (2020).
17. Z. Li, K. G. Pradeep, Y. Deng, D. Raabe, C. C. Tasan, Metastable high-entropy dual-phase alloys overcome the strength-ductility trade-off. *Nature* **534**, 227–230 (2016).
18. S. Chen, H. S. Oh, B. Gludovatz, S. J. Kim, E. S. Park, Z. Zhang, R. O. Ritchie, Q. Yu, Real-time observations of TRIP-induced ultrahigh strain hardening in a dual-phase CrMnFeCoNi high-entropy alloy. *Nat. Commun.* **11**, 826 (2020).
19. S. W. Wu, G. Wang, Q. Wang, Y. D. Jia, J. Yi, Q. J. Zhai, J. B. Liu, B. A. Sun, H. J. Chu, J. Shen, P. K. Liaw, C. T. Liu, T. Y. Zhang, Enhancement of strength-ductility trade-off in a high-entropy alloy through a heterogeneous structure. *Acta Mater.* **165**, 444–458 (2019).
20. P. Shi, W. Ren, T. Zheng, Z. Ren, X. Hou, J. Peng, P. Hu, Y. Gao, Y. Zhong, P. K. Liaw, Enhanced strength-ductility synergy in ultrafine-grained eutectic high-entropy alloys by inheriting microstructural lamellae. *Nat. Commun.* **10**, 489 (2019).
21. J. Ren, Y. Zhang, D. Zhao, Y. Chen, S. Guan, Y. Liu, L. Liu, S. Peng, F. Kong, J. D. Poplawsky, G. Gao, T. Voisin, K. An, Y. M. Wang, K. Y. Xie, T. Zhu, W. Chen, Strong yet ductile nanolamellar high-entropy alloys by additive manufacturing. *Nature* **608**, 62–68 (2022).
22. W.-R. Wang, W.-L. Wang, S.-C. Wang, Y.-C. Tsai, C.-H. Lai, J.-W. Yeh, Effects of Al addition on the microstructure and mechanical property of $Al_xCoCrFeNi$ high-entropy alloys. *Intermetallics* **26**, 44–51 (2012).
23. Q. Zhang, R. Huang, J. Jiang, T. Cao, Y. Zeng, J. Li, Y. Xue, X. Li, Size effects and plastic deformation mechanisms in single-crystalline CoCrFeNi micro/nanopillars. *J. Mech. Phys. Solids* **162**, 104853 (2022).
24. Q. Zhang, R. Huang, X. Zhang, T. Cao, Y. Xue, X. Li, Deformation mechanisms and remarkable strain hardening in single-crystalline high-entropy-alloy micropillars/nanopillars. *Nano Lett.* **21**, 3671–3679 (2021).
25. J. Li, Q. Fang, B. Liu, Y. Liu, Transformation induced softening and plasticity in high entropy alloys. *Acta Mater.* **147**, 35–41 (2018).
26. S. Chen, Z. H. Aitken, S. Pattamatta, Z. Wu, Z. G. Yu, R. Banerjee, D. J. Srolovitz, P. K. Liaw, Y.-W. Zhang, Chemical-affinity disparity and exclusivity drive atomic segregation, short-range ordering, and cluster formation in high-entropy alloys. *Acta Mater.* **206**, 116638 (2021).
27. C. Jiang, B. P. Uberuaga, Efficient ab initio modeling of random multicomponent alloys. *Phys. Rev. Lett.* **116**, 105501 (2016).
28. V. Sorkin, S. Chen, T. L. Tan, Z. G. Yu, M. Man, Y.-W. Zhang, First-principles-based high-throughput computation for high entropy alloys with short range order. *J. Alloys Compd.* **882**, 160776 (2021).
29. Z. Fu, W. Chen, H. Wen, D. Zhang, Z. Chen, B. Zheng, Y. Zhou, E. J. Lavernia, Microstructure and strengthening mechanisms in an FCC structured single-phase nanocrystalline $Co_{25}Ni_{25}Fe_{25}Al_{7.5}Cu_{17.5}$ high-entropy alloy. *Acta Mater.* **107**, 59–71 (2016).
30. X. W. Zhou, R. A. Johnson, H. N. G. Wadley, Misfit-energy-increasing dislocations in vapor-deposited CoFe/NiFe multilayers. *Phys. Rev. B* **69**, 144113 (2004).
31. S. Chen, Z. H. Aitken, Z. Wu, Z. Yu, R. Banerjee, Y.-W. Zhang, Hall-Petch and inverse Hall-Petch relations in high-entropy $CoNiFeAl_xCu_{1-x}$ alloys. *Mater. Sci. Eng. A* **773**, 138873 (2020).
32. S. Liu, Y. Wei, The Gaussian distribution of lattice size and atomic level heterogeneity in high entropy alloys. *Extreme Mech. Lett.* **11**, 84–88 (2017).
33. A. J. Zaddach, C. Niu, C. C. Koch, D. L. Irving, Mechanical properties and stacking fault energies of NiFeCrCoMn high-entropy alloy. *JOM* **65**, 1780–1789 (2013).
34. Y. Deng, C. C. Tasan, K. G. Pradeep, H. Springer, A. Kostka, D. Raabe, Design of a twinning-induced plasticity high entropy alloy. *Acta Mater.* **94**, 124–133 (2015).
35. D. Faken, H. Jónsson, Systematic analysis of local atomic structure combined with 3D computer graphics. *Comput. Mater. Sci.* **2**, 279–286 (1994).
36. A. Stukowski, V. V. Bulatov, A. Arsenlis, Automated identification and indexing of dislocations in crystal interfaces. *Model. Simul. Mat. Sci. Eng.* **20**, 085007 (2012).
37. A. Stukowski, Visualization and analysis of atomistic simulation data with OVITO-the open visualization tool. *Model. Simulat. Mater. Sci. Eng.* **18**, 15012 (2009).
38. J. S. Bowles, C. M. Wayman, The Bain strain, lattice correspondences, and deformations related to Martensitic transformations. *Metall. Trans.* **3**, 1113–1121 (1972).
39. E. H. Ekiz, T. G. Lach, R. S. Averback, N. A. Mara, I. J. Beyerlein, M. Pouryazdan, H. Hahn, P. Bellon, Microstructural evolution of nanolayered Cu–Nb composites subjected to high-pressure torsion. *Acta Mater.* **72**, 178–191 (2014).
40. J. S. Carpenter, T. Nizolek, R. J. McCabe, M. Knezevic, S. J. Zheng, B. P. Eftink, J. E. Scott, S. C. Vogel, T. M. Pollock, N. A. Maraa, I. J. Beyerlein, Bulk texture evolution of nanolamellar Zr–Nb composites processed via accumulative roll bonding. *Acta Mater.* **92**, 97–108 (2015).
41. S. Wei, L. Zhang, S. Zheng, S. Wang, X. Wang, J. Wang, Deformation-induced interfacial transition zone in Cu/V nanolamellar multilayers. *Scr. Mater.* **159**, 104–108 (2019).
42. Y. T. Zhu, X. Liao, Retaining ductility. *Nat. Mater.* **3**, 351–352 (2004).
43. Z. Budrovic, H. Van Swygenhoven, P. M. Derlet, S. Van Petegem, B. Schmitt, Plastic deformation with reversible peak broadening in nanocrystalline nickel. *Science* **304**, 273–276 (2004).
44. Y. Zhang, J. G. Gigax, T. J. Nizolek, J. S. Carpenter, M. M. Schneider, N. Li, L. Capolungo, R. J. McCabe, Tensile and failure behaviors of Cu/Nb nanolaminates: The effects of loading direction, layer thickness, and annealing. *Acta Mater.* **240**, 118346 (2022).
45. L. Fan, T. Yang, Y. Zhao, J. Luan, G. Zhou, H. Wang, Z. Jiao, C.-T. Liu, Ultrahigh strength and ductility in newly developed materials with coherent nanolamellar architectures. *Nat. Commun.* **11**, 6240 (2020).
46. A. Misra, J. P. Hirth, R. G. Hoagland, Length-scale-dependent deformation mechanisms in incoherent metallic multilayered composites. *Acta Mater.* **53**, 4817–4824 (2005).
47. B. Cantor, G. A. Chadwick, The tensile deformation of unidirectionally solidified Al-Al_3Ni and Al-Al_2Cu eutectics. *J. Mater. Sci.* **10**, 578–588 (1975).
48. J. Tian, Y. Zhao, H. Hou, P. Han, First-principles investigation of the structural, mechanical and thermodynamic properties of Al_2Cu phase under various pressure and temperature conditions. *Solid State Commun.* **268**, 44–50 (2017).
49. H. M. Otte, W. G. Montague, D. O. Welch, X-Ray Diffractometer determination of the thermal expansion coefficient of aluminum near room temperature. *J. Appl. Phys.* **34**, 3149–3150 (1963).
50. S. Plimpton, Fast parallel algorithms for short-range molecular dynamics. *J. Comput. Phys.* **117**, 1–19 (1995).
51. G. Kresse, J. Furthmüller, Efficient iterative schemes for ab initio total-energy calculations using a plane-wave basis set. *Phys. Rev. B* **54**, 11169–11186 (1996).
52. P. E. Blöchl, Projector augmented-wave method. *Phys. Rev. B* **50**, 17953–17979 (1994).
53. G. Kresse, D. Joubert, From ultrasoft pseudopotentials to the projector augmented-wave method. *Phys. Rev. B* **59**, 1758–1775 (1999).
54. J. P. Perdew, K. Burke, M. Ernzerhof, Generalized gradient approximation made simple. *Phys. Rev. Lett.* **77**, 3865–3868 (1996).
55. B. Yaakobi, T. R. Boehly, D. D. Meyerhofer, T. J. B. Collins, B. A. Remington, P. G. Allen, S. M. Pollaine, H. E. Lorenzana, J. H. Eggert, EXAFS measurement of iron bcc-to-hcp phase transformation in nanosecond-laser shocks. *Phys. Rev. Lett.* **95**, 075501 (2005).
56. Y. Ping, F. Coppari, D. G. Hicks, B. Yaakobi, D. E. Fratanduono, S. Hamel, J. H. Eggert, J. R. Rygg, R. F. Smith, D. C. Swift, D. G. Braun, T. R. Boehly, G. W. Collins, Solid iron compressed up to 560 GPa. *Phys. Rev. Lett.* **111**, 065501 (2013).

Acknowledgments: We gratefully acknowledge the use of computing resources at the A*STAR Computational Resource Centre and National Supercomputer Centre, Singapore. This work is also supported by Shanghai Technical Service Center of Science and Engineering Computing, Shanghai University. **Funding:** This work was funded by Shanghai Pujiang Program grant 22PJ1403700 (S.C.); National Natural Science Foundation of China grant 52301017 (S.C.); Agency for Science, Technology and Research (A*STAR) grant AMDM A1898b0043 (Y.-W.Z.); Research Grants Council of the Hong Kong Special Administrative Region, China grant 11211019 (D.J.S.); National Science Foundation grant DMR-1611180, 1809640, and 2226508 (P.K.L.); and U.S. Army Research Office grants W911NF-13–1-0438 and W911NF-19–2-0049 (P.K.L.). **Author contributions:** Conceptualization: S.C., P.L., and Y.-W.Z. Methodology: S.C., P.L.,

and Q.P. Investigation: S.C. and Y.-W.Z. Visualization: S.C. and P.L. Supervision: D.J.S., P.K.L., and Y.-W.Z. Writing—original draft: S.C., P.L., and Y.-W.Z. Writing—review and editing: S.C., P.L., Q.P., Z.-G.Y., Z.H.A., W.L., Z.W., R.B., D.J.S., P.K.L., and Y.-W.Z. **Competing interests:** The authors declare that they have no competing interests. **Data and materials availability:** All data needed to evaluate the conclusions in the paper are present in the paper and/or the Supplementary Materials. Data S1 contains source files for MD simulations.

Submitted 5 May 2023
Accepted 11 September 2023
Published 13 October 2023
10.1126/sciadv.adi5817